AIAA'85

AIAA-85-0974

Heating Rate Distributions at Mach 10 on a Circular Body Earth-to-Orbit Transport Vehicle

William L. Wells, Ian O. MacConochie,
Vernon T. Helms III, and David Raney
NASA Langley Research Center,
Hampton, Virginia

AIAA 20th Thermophysics Conference
June 19-21, 1985 / Williamsburg Virginia

HEATING RATE DISTRIBUTIONS AT MACH 10 ON A CIRCULAR BODY EARTH-TO-ORBIT TRANSPORT VEHICLE

William L. Wells*, Ian O. MacConochie†,
Vernon T. Helms III*, and David Raney**
NASA Langley Research Center
Hampton, Virginia 23665

Abstract

Among the concepts being considered for future Earth-to-orbit transport vehicles are fully reusable single-stage systems which take off vertically and land horizontally. Because these vehicles carry their own propellant internally, they are much larger than the present Space Shuttle Orbiter. One such single-stage vehicle under study is the circular body configuration which has the advantages of simple structural design and large volume-to-weight ratio. As part of an overall evaluation of this configuration, a series of heat transfer and surface flow tests were conducted. The phase-change paint and oil-flow tests were performed in the Langley 31-Inch Mach-10 Tunnel at angles of attack from 20 through 40 degrees in 5-degree increments. Heat-transfer coefficient data are presented for all angles of attack and detailed oil-flow photographs are shown for windward and leeward surfaces at 25 and 40 degrees angle of attack. In many ways, heating was similar to that previously determined for the Shuttle Orbiter so that, in a cursory sense, existing thermal protection systems would appear to be adequate for the proposed circular-body configurations.

Introduction

Weight is very critical to the overall system efficiency of Earth-to-orbit transport vehicles. For every kilogram of structural weight saved in a single-stage vehicle, overall weight can be reduced by approximately 35 kilograms. Since a circular cross-section body is one of the most efficient structural shapes, this configuration was selected for investigation and is the subject of this heating study.

Planform loading and surface curvature are important factors in entry heating. Since Earth-to-orbit transports proposed for the future do not have expendable external fuel tanks. these vehicles will be large even in comparison to the Space Shuttle Orbiter and will principally consist of very large integral tanks to carry propellant for the main rocket engines. In contrast to the Shuttle Orbiter. the cargo and crew compartments make up a very small fraction of the internal volume (and weight) of the vehicle. As a consequence of its large size and low entry weight (relative to size), the planform loading for this family of vehicles at entry is low. A circular body vehicle (CBV), for example, sized to return a 30,000 kg payload, has an entry planform loading approximately 26 percent lower than the Shuttle. Some approximate dimensions for such a CBV configuration would be 60-m long, 10-m diameter, and a 40-m wing span.

In addition to the use of a simple circular cross section for most of the body, no canopy would be provided for the pilots and crew. Instead. the crew compartment and payload bay would be located in the mid fuselage. Flush viewing ports could be used for on-orbit visibility while a nose gear deployed TV camera and auto-pilot would be employed for landing.

With these major differences in shape and planform loading as a background, the objective of this study is to determine the viability of a circular cross-section body for the Earth-to-orbit transport application from the standpoint of heating. As part of a larger overall investigation of the CBV configuration, both phase-change paint and oil-flow techniques were utilized to identify surface flow patterns and heating-rate distributions at Mach 10, and these results are presented here.

Symbols

c	specific heat of model material, J/kg-K
f	correction factor for heat-transfer coefficient on leeward thin sections; see Fig. 2.
h	local heat-transfer coefficient, W/m-K
h_o	stagnation heat-transfer coefficient on a scaled 1-foot radius sphere in the freestream, W/cm^2K
k	thermal conductivity of model material, W/m-K
L	model length, m
M	freestream Mach number, dimensionless
N_{Re}	Reynolds number, m^{-1}

*Aero-Space Technologist, Aerothermodynamics Branch, Space Systems Division.
†Aero-Space Technologist, Vehicle Analysis Branch, Space Systems Division. Member AIAA.
**Engineering Co-Op Student, University of Cincinnati. Cincinnati. Ohio.

N_{Pr}	Prandtl number, dimensionless
$\dot{q}$	heating rate, W/m^2
r	radius, m
r_c	recovery factor, dimensionless
t	time, s
T	temperature, K
$\bar{T}$	temperature ratio defined by Eq. (2)
x	longitudinal distance from model nose, m
Y	spanwise distance from model centerline, m
α	angle attack or thermal diffusivity, degrees or m^2/s
β	defined by Eq. (1), $W\text{-}s^{1/2}/m^2\text{-}K$
γ	ratio of specific heats for air
ϕ	angle shown in Fig. 19, degrees
ρ	model material density, kg/m^3

Subscripts

aw	adiabatic wall
℄	centerline
i	initial
o	stagnation value
∞	freestream value

Models

The 0.0055-scale Stycast model used in these tests is shown in Figs. 1(a), (b), (c), and (d). (Stycast is a product of Emerson and Cuming, Inc.) Its overall length from nose to elevon hinge line is 33.02 cm, and the nose radius is 0.64 cm. The ogive forebody section is formed using a constant radius of 23.88 cm centered on a line perpendicular to the vehicle body axis at x/L = 0.31. The constant cylindrical portion of the body (2.745-cm radius) extends from x/L = 0.31 to 0.54. At the latter station, the wing-body transition section is started. The constant radius circular cross section continues to the base of the model, and it is blended to the wing by flat vertical surfaces.

The wing is a clipped delta design with a 47-degree leading edge sweep and a zero-degree trailing edge sweep. Wing incidence is 1.5-degrees, and the dihedral is 7 degrees. The basic wing airfoil shape is a NACA-0010-64 and is constant from root to tip. For these heating tests, however, the wing was thickened to improve the semi-infinite slab approximation imposed by the heating analysis and to provide increased resistance to structural damage due to thermal stresses. This thickening starts on the wing's upper surface at the maximum chord thickness and extends to the trailing edge as shown in Fig. 1(b). The wing-tip fins are formed from flat-sided wedges with rounded leading edges that are swept at 30-degrees, have an outboard cant angle of 10 degrees, and a toe angle of 1.5 degrees. Both wing-tip fins have a trailing edge thickness of 0.3175 cm, but the leading edge radius of the left fin is 0.1143 cm while the right fin radius is 0.0762 cm. The leading edge radius and base thickness are constant from root to tip on each fin.

Several identical models were made since charring of the model material occurred in areas of high heating after a number of tests.

Scope of Tests

The tests were conducted in air in the Langley 31-Inch Mach 10 Tunnel. The models were tested in two flow environments characterized by freestream Reynolds numbers ($N_{Re,\infty}$) of 1.64×10^6 m^{-1} and 3.28×10^6 m^{-1}. Most of the heating tests were made at $N_{Re,\infty} = 3.28 \times 10^6$ m^{-1} with angles of attack from 20 to 40 degrees in 5-degree increments. A more limited number of oil-flow tests were made. The test conditions are summarized in Table 1.

Heat-Transfer Measurement Technique

The phase-change paint technique was used to determine the heat-transfer coefficient for this series of tests. This technique employs a series of paints that melt, or change phase, at known temperatures. Typically, a thin coat of opaque light-colored paint is sprayed on a dark-colored model. The paint becomes transparent when melted. Knowledge of the model material properties, the time required to melt the paint, and the paint melt-temperature provides sufficient information to determine the heat-transfer coefficient at a particular location. Reference 1 presents a comprehensive discussion of this technique. Those portions that are directly applicable to this study are briefly discussed here.

Mathematical relations for determining the heat transfer coefficient can be derived from the equations governing transient one-dimensional heat conduction into a semi-infinite slab. These derived relations are

$$\bar{T} = 1 - e^{\beta^2} \operatorname{erfc} \beta \qquad (1)$$

where

$$\bar{T} = \frac{T_{pc} - T_i}{T_{aw} - T_i} \qquad (2)$$

and $$\beta = \frac{h}{k}\sqrt{\alpha t} \quad \text{or} \quad h = \beta\sqrt{\frac{\rho c k}{t}}, \text{ since } \alpha = \frac{k}{\rho c} \qquad (3)$$

The model material properties parameter $\sqrt{\rho c k}$ is usually determined experimentally by use of the heating device described in Ref. 2. This device was inoperative at the time of these tests; therefore, a value of 1596 $\frac{W\text{-}sec^{1/2}}{m^2K}$ was used since this value was recently determined for

other models that were cast from the same batch of stycast material and by the same craftsmen. Equations (1) and (2) were used to determine β, and the time t required to melt the paint at a particular location was determined from motion-picture film exposed during a test. The adiabatic wall temperature in equation (2) was obtained from

$$T_{aw} = \frac{T_{aw}}{T_t} T_t = \frac{1 + r_c (\frac{\gamma-1}{2})M^2}{1 + (\frac{\gamma-1}{2})M^2} T_t$$

$$= \frac{1 + \sqrt{N_{Pr}} (\frac{\gamma-1}{2})M^2}{1 + (\frac{\gamma-1}{2})M^2} T_t \qquad (4)$$

which assumes a constant property, laminar boundary layer flow condition. The total temperature T_t was obtained from wind-tunnel thermocouples. and the model initial temperature T_i was measured by a thermocouple imbedded in the model. Enough time was allowed between tests for T_i to return to the ambient temperature.

For a particular test, a paint was selected with a phase-change temperature that would allow the data to be obtained before the thermal diffusion time was exceeded in a particular section of the model wall. This requirement derives from a boundary condition imposed by the original semi-infinite slab approximation.[1]

The motion-picture camera used to record the data was operated at a rate of 10 frames per second. A stroboscopic lamp was used to illuminate the model, and the pulse rate was synchronized with the camera framing rate. Continuous operating high-intensity lamps can add a significant radiant heat load to the model.[1]

Heat Transfer Data Reduction

From images recorded on motion picture film. the boundary between melted and unmelted paint at a particular time during a test was superimposed on an outline of the model. This boundary represents a contour line of constant heating rate that is determined by the heat-transfer measurement technique previously discussed. At a later test time the new melt boundary, representing a lesser heating rate, was also superimposed onto the model outline, and so on, until a heating-rate contour map of the surface of interest was obtained. The area between two contour lines has heating rates that have upper and lower limits defined by the two lines. The data presented here are in terms of the heat-transfer coefficient (h) that has been nondimensionalized by the theoretical stagnation-point heat-transfer coefficient (h_o) for a 1-ft radius sphere at the model scale and test conditions. The heating rate, q, can be related to the heat-transfer coefficient by:

$$\dot{q} = h(T_{aw}-T) \qquad (5)$$

where T is the local surface temperature which is given by the melting temperature of the phase change paint for the particular test of interest.

The phase change data reduction technique is applicable to all areas on the fuselage. However, the assumption of a thick-body can be violated on thin sections such as wings and fins. Reference 3 provides a method of computing correction factors for the effect of thin model segments. A general assessment was made of correction factors required for different areas of the wings and fins rather than making detailed calculations to determine corrected heating distributions. Thermal diffusion time, which depends on material properties and thickness, and the phase change paint melt time at the same chordwise and spanwise locations are the key parameters used to determine the correction factors. Wing windward surface phase change paint melting usually occurred earlier than on the wing's leeward surface for a given axial and spanwise location. This resulted in the wing windward surface correction factor varying from 1.0 by only a few percent at some locations so that essentially no correction is required for the wing windward surface heating data in this report. Correction factors for different areas on the wing upper surface are presented in Fig. 2. The numbers shown on each portion of the wing represent average correction factors for the indicated areas. Short melt times near the wing leading edge resulted in only a small correction to the semi-infinite slab data obtained there. A progressively larger change is required in approaching the wing-tip and the trailing edge due to a combination of low thermal diffusion times and long melt times. However, there are some cases in the data where wing leeward surface phase change melting occurred very rapidly in response to high heating rates in confined regions extending from forward wing locations to the trailing edge. In such cases, the correction factor which should be used over the extent of the contour is more nearly equal to the correction factor affecting its most forward position as determined from Fig. 2. Since the correction factor varies over the wing upper surface, it is not evident that the leeside heating distribution is represented by the isotherm contour map. To provide a "quick look" representation of the heating distribution, the data on the right-hand wing were digitized and multiplied by the appropriate correction factor. From these data, a few constant h/h_o contour lines were then sketched onto the right-hand wing. Areas of the wing that are shaded indicate regions where the paint did not melt so that only the value of h/h_o at the melt boundary is indicated. The data were symmetrical with respect to the left and right wings; therefore, the view of the left wing presents the original uncorrected isotherm contour map. A constant correction factor of 0.4 was found to be a representative value for the thin tip-fin sections, and this correction has been made to the contour data shown in the appropriate figures.

Factors affecting data accuracy are discussed at length in Ref. 1. These factors are too numerous and variable to elaborate on in this paper but include model injection time, time at which data is read, difference in initial temperature and phase-change temperature, known value of T_{pc}, model material properties, and determination of initial time of heating (t=0). Model illumination, camera viewing angle, and the

heating gradient over a particular surface area were also found to affect the accuracy with which the data could be read from the film. Other types of heating data are not presently available for this configuration; however, there are data for the extensively studied Space Shuttle Orbiter configuration. One recent set of phase-change heating tests using the shuttle configuration in the same facility and over the same test range as the present tests showed that the phase-change data compared to within 5 percent of theoretical values and similar thermocouple (thin-skin) data over most of the model length along the windward centerline.[4] Data along the windward centerline of the present model are considered to be of similar accuracy since model material and length, facility, test range, equipment, and technical personnel were the same in both cases. In off-centerline regions and on leeward surfaces where heating is less uniform, however, the data are expected to be less accurate. Traditionally, heat-transfer data with accuracies better than 20 percent have been difficult to obtain under similar circumstances. Because the film read-up phase of the present data reduction is somewhat subjective, accuracies better than this probably should not be claimed. Furthermore, heating data on the wing leeside and on the wing-tip fins should be considered qualitative rather than quantitative. Use of the multiplying factors from Fig. 2, however, provides at least some degree of quantitative results. Paint melt occurs too soon after model injection for practical data read-up on the nose and leading edges of the wings and fins.

Oil-Flow Technique and Data Reduction

Oil-flow tests were run with the same red Stycast model used in the phase change paint experiments. The oil is a mixture of Dow Corning clear silicon fluid and Liquitex Artist Oil Color (Zinc Everwhite). Mixtures were prepared using fluids with viscosities of 10 centistokes (cs) 50 cs, 100 cs, 200 cs, and 350 cs. A thin base coat of clear 10 cs fluid was brushed onto all parts of the model, except the windward surfaces at very high angles of attack, to act as a lubricant for the oil mixtures. The mixtures were applied to the model by rapidly stroking the end of a small, stiff, oil-ladened brush with the forefinger to produce a thick array of white spots on the model's surface. Oil mixtures of different viscosities were used on different parts of the model in accordance with local surface shear. The low viscosity 10 cs mixture was used on leeward surfaces where flow separation occurs and on the inside of the tip fin. It was also used in combination with the 50 cs mixture on the tip fin exterior surface and on the side fuselage above the wing. The 50 cs mixture was required on the wing leeside attached flow region. Both 50 cs and 100 cs mixtures were used on the side fuselage ahead of the wing. The high viscosity 200 cs and 350 cs mixtures were used almost exclusively on windward areas. The thickness of the base coat as well as the correct ratio of one mixture to another on a given portion of the model must be determined experimentally.

Wind-Tunnel Description

The Langley 31-Inch Mach 10 Tunnel (formerly, the Continuous Flow Hypersonic Tunnel) was used for the test series reported here. A test time of at least 30 seconds was available. The tunnel uses dry air which is heated to the total temperature by electrical resistance heaters. A fixed geometry, three-dimensional, contoured nozzle with a 31-inch (0.79 m) square test section provides a nominal Mach number of 10. The usable test core varies from 30.5 cm square at $N_{Re,\infty} = 1.31 \times 10^6$ m^{-1} to 36.8 cm square at $N_{Re,\infty} = 7.87 \times 10^6$ m^{-1}. The sidewall-mounted injection system requires approximately 0.5 sec to inject the model to the stream centerline. A more detailed description of this facility can be found in Ref. 5.

Discussion of Results

Model outlines with contours representing lines of constant heat transfer coefficient were obtained by the phase-change paint technique. These heat-transfer coefficient contour maps are presented in Figs. 3-7 for $N_{Re,\infty} = 3.28 \times 10^6$ m^{-1} and angles of attack of 20, 25, 30, 35, and 40 degrees. Figure 8 presents contour data for $N_{Re,\infty} = 1.64 \times 10^6$ m^{-1} and $\alpha = 30$ degrees. Each figure (3 through 8) has three parts; (a) bottom view, (b) side view, and (c) top view. Some areas of the model experienced heating rates that were too high to be recorded by the phase-change paint technique. These areas were the nose, the leading edges of the wing, and wing tip fins. Although heating values were not obtained for these areas, it should be kept in mind that the values will be higher than any other values shown in the figures. Based on charring of the model material, one of the regions of highest heating occurred where the bow shock impinged on the leading edge of the wing at about 1/3 semi-span. Some regions of the wing and tip fins were too thin to allow the semi-infinite slab approximation as required by the heating analysis used here. Recall that multiplying factors are supplied in Fig. 2 to correct for values in these regions. Because of space limitations here, not all of the heating contour figures will be discussed. Some of the prominent heating features will be discussed along with the presentation of related oil-flow results in the following paragraphs.

Surface flow visualization using the oil-flow technique was performed to aid interpretation of the phase change paint heating contours. A series of oil-flow photographs showing surface flow patterns that are representative of the low and the high angles of attack used in the present study are included. Direct comparisons between oil-flow patterns and phase change paint heating contours obtained at $N_{Re,\infty} = 3.28 \times 10^6$ m^{-1} are presented. Figures 9(a) and 9(b) show windward surface oil-flow patterns on the circular body vehicle at $\alpha = 25°$ and 40°, respectively. Similar surface flow patterns exist on the model's forward fuselage at both angles of attack except for the expected greater flow divergence

at $\alpha = 40°$. Major differences in the oil flow can be seen on the wing windward surface in these two figures. Effects of shock interactions are evident at $\alpha = 25°$ in the form of streaks and other irregularities in the oil flow, but the results at $\alpha = 40°$ show a uniform surface flow pattern. Oil-flow feature "A" identified in both Figs. 9(a) and 9(b) shows surface patterns associated with formation of the wing shock. The resultant large pressure gradient turns the local flow inboard to a greater degree at $\alpha = 25°$ than at $\alpha = 40°$. The label "B" in Fig. 9(a) marks the location of the bow-shock/wing-shock intersection.

There are no obvious shock interaction effects on the wing lower surface at $\alpha = 40°$ because the increased shock layer thickness at high incidence decreases the intensity of the interaction and blends the transmitted effects into the general flowfield before reaching the surface. The locus of points defining an expansion fan, feature "C," at $\alpha = 25°$ in Fig. 9(a) can be seen radiating inboard and downstream from the shock intersection on the wing leading edge. Close examination of the oil flow reveals that the generally inboard surface flow directions ahead of feature "C" are turned in a more downstream or slightly outboard direction aft of it. This is the result of flow expansion near the surface which may be caused by a Type VI shock interaction as defined in Ref. 6. The expansion fan dissipates well outboard of the model's windward centerline as it approaches the symmetry plane flow.

Feature "D" in Fig. 9(a) also originates at the bow-shock/wing-shock interaction on the wing leading edge, and it appears to be a vortex-like reattachment. Surface flow outboard of "D" travels in a streamwise and slightly outboard direction parallel to the reattachment line, whereas flow inside of feature "D" immediately turns inboard. A small spanwise segment of the wing outboard of feature "D" is occupied by alternating light and dark streaks in the oil flow. This band of streaks, identified as feature "E" in Fig. 9(a), can be traced forward to the wing leading edge in the vicinity of the bow-shock/wing-shock intersection. These streaks may result from embedded vortices which are induced by large pressure gradients propagating downstream from the shock intersection similar to that which was observed on an early shuttle orbiter configuration (Ref. 7). Features "C," "D," and "E" disappeared for $\alpha > 30°$ and they are not present in Fig. 9(b).

The oil flows shown in Figs. 9(a) and 9(b) are the result of tests at the same conditions as the phase change paint results presented in Figs. 4(a) and 7(a) for $\alpha = 25°$ and $\alpha = 40°$, respectively. The letter designations in these figures indicate heating contours corresponding to surface flow patterns identified by the same letters in Fig. 9. Figure 4(a) shows that there is a decrease in the wing spanwise heating across the expansion fan, feature C, as expected (Ref. 8). The vortex-like reattachment, feature D, in Fig. 4(a) produces values of $h/h_o > 0.056$ which represents a significant enhancement over heating in adjacent areas. The embedded vortices at $\alpha = 25°$, labeled "E," also result in locally higher heating as evidenced by fluctuations in the phase change paint contours outboard of feature "D." A segment of nearly constant heating is located along the windward centerline in Fig. 4(a) between the model's ogive forebody and the wing which is apparently the result of a swept cylinder type flowfield on that portion of the circular body vehicle. Also, small regions of relatively high heating are concentrated in areas where the wing leading edge blends with the circular fuselage. Perhaps a smoother blending of wing and body could reduce heating in these regions. Approximately the same windward centerline locations experience nearly constant heating at $\alpha = 40°$ in Fig. 7(a) and the wing-body blending also produces slightly elevated heating rates. The remainder of the phase change contours in Fig. 7(a) are almost featureless except for the wedge of higher heating which propagates from the vicinity of the bow-shock/wing-shock interaction and the wing-shock formation.

Flow reattachment which occurs above the wing is an area of interest on the model's side fuselage. Figures 10(a) and 10(b) show the associated oil-flow patterns at $\alpha = 25°$ and 40°, respectively. The reattachment locations at these two angles of attack are indicated by the dashed lines. Reattachment begins just aft of the concave segment which blends the wing and fuselage, and it occurs higher on the side fuselage with increasing angle of attack. A clearly defined reattachment location was not detected aft of the dashed lines. The separation line which forms the upper boundary of the reattachment-related upwash pattern at aft locations on the model is forced farther downward onto the side fuselage in Fig. 10(b) than in Fig. 10(a) due to a more complex leeward fuselage flow pattern at high angles of attack. Also in Fig. 10(b), the aft portion of the side fuselage reattachment pattern is bordered by a pocket of flow with upward and streamwise components located above the wing near the model's base. This flow also influences wing leeward surface patterns that will be discussed later. Figure 10(a) shows what appears to be a similar but much smaller flow pocket at $\alpha = 25°$. An overall view of oil-flow patterns on the model's side fuselage at $\alpha = 40°$ is shown in Fig. 10(c). The only significant difference in forward fuselage oil-flow patterns at lower angles of attack compared to those shown here is a decrease in the inclination of surface flow directions with respect to the model's axis.

Figures 4(b) and 7(b) show phase change paint heating contours on the side fuselage and tip fin of the model at $\alpha = 25°$ and 40°, respectively. Side fuselage contours caused by flow reattachment above the wing extend to the end of the model in Fig. 4(b), but not in Fig. 7(b); that is, paint did not melt in the aft region. This may be partially due to the aft constriction of the reattachment flow pattern at $\alpha = 40°$ shown in Fig. 10(b). The vertical placement of peak heating in the contours above the wing in Fig. 7(b) clearly indicates a rise in the location of the side fuselage reattachment at $\alpha = 40°$ compared to that for $\alpha = 25°$ in Fig. 4(b), in agreement with the oil-flow analysis. Heating on the outboard surface of the tip fin is highlight-

ed by a narrow corridor of locally enhanced heating that is oriented diagonally upward across the structure at an angle that becomes larger with increasing angle of attack. Heating within this corridor at $\alpha = 40°$ appears to be approximately twice that for $\alpha = 25°$.

Oil-flow patterns on the tip-fin outboard surface presented in Figs. 11(a) and 11(b) correspond to the phase change results of Figs. 4(b) ($\alpha = 25°$) and 7(b) ($\alpha = 40°$), respectively. These data show that the corridor of locally enhanced heating is caused by vortex reattachment. The reattachment line leaves the tip-fin trailing edge at 46 percent of its span for $\alpha = 25°$ and at 77 percent of span for $\alpha = 40°$. These are the same locations indicated by the phase change measurements in Figs. 4(b) and 7(b). The reattachment originates lower on the tip fin's leading edge at lower angles of attack and it may be caused by impingement of the wing shock. Flow above the reattachment line sweeps aft and upward. Below the reattachment line flow turns in a streamwise and slightly downward direction. The downward-moving flow separates near the base of the tip fin upon encountering upward-moving flow from the wing windward surface. These reattachment oil-flow patterns are similar to those found on a proposed tip-fin configuration for the Space Shuttle Orbiter in Ref. 9.

Leeside oil-flow patterns for $\alpha = 25°$ are shown in Fig. 12(a) and those for $\alpha = 40°$ are in Fig. 12(b). (Keep in mind that the wing upper surface has been modified from the chord line to the trailing edge on this model; see "Models" section. The flow may be different to some extent on the true wing shape.) In both cases, a single vortex pair produces flow reattachment on the model's leeward centerline. The reattachment extends over essentially the entire length of the model at $\alpha = 25°$. At $\alpha = 40°$, a very complex leeside separated flow pattern that was mentioned with regard to Fig. 10(b) terminates the vortex reattachment near $x/L = 0.7$. The lack of oil movement aft of $x/L = 0.7$ in Fig. 12 is indicative of low shear associated with the separated flow dominating that portion of the fuselage. Wing leeward surface oil-flow patterns in Figs. 12(a) and 12(b) are greatly different. There is a large area of attached flow at $\alpha = 25°$ and an equally large area of flow separation with intricate reattachment patterns at $\alpha = 40°$.

Figures 13(a) and 13(b) show closeup photographs of the wing leeside oil-flow results at $\alpha = 25°$ and 40°, respectively. The slender wedge of slightly outboard flow close to the fuselage in Fig. 13(a) is a result of the vortex which causes the side fuselage reattachment shown in Fig. 10(a). A line of flow separation divides the wedge-shaped area from attached flow emmanating from the wing leading edge. There is an additional separation at the aft end of the wedge-shaped area caused by interaction with forward-moving flow originating near the model's base. There appears to be a shock-induced separation causing flow reattachment beginning near the wing's mid-section in Fig. 13(a) which travels outboard as it moves downstream. There is a pocket of reversed flow caused by flow reattachment near the wing trailing edge just inboard of the tip fin. Also, a disturbance in the wing upper surface flow pattern can be seen in the vicinity of the tip-fin leading edge. The oil-flow test at $\alpha = 40°$, shown in Fig. 13(b), reveals a truncated wedge-shaped area of outflow from the side fuselage vortex which borders with a small region of attached flow from the inboard portion of the wing leading edge. Aft of these areas, a very large pattern of generally forward moving flow radiates from a flow reattachment point near the wing trailing edge. The inboard component of this pattern is the source of the side fuselage flow pocket previously shown in Fig. 10(b). Flow reattachment also occurs on the wing upper surface near the tip fin. Flow from this feature forms a separation line where it meets outward flow from the large inboard reattachment pattern. The outboard reattachment also directs flow forward to a separation line aft of the wing leading edge.

Figure 14 shows closeup photographs of oil-flow patterns on the tip-fin inboard surface and on the adjacent upper surface of the wing. Flow reattachment on the outbound segment of the wing trailing edge at $\alpha = 25°$ in Fig. 14(a) influences flow on the lower aft portion of the tip fin. Separation occurs upon meeting the generally streamwise flow which dominates the tip-fin inboard surface at low to moderate angles of attack. The wing-tip reattachment described in Fig. 13(b) for $\alpha = 40°$ is shown to originate on the tip-fin inboard surface in Fig. 14(b) where approximately one-half of the tip-fin area is occupied by this flow pattern. The upper portion of the tip fin still retains attached flow which joins the reattachment flow pattern along a separation line running diagonally across the structure.

Phase change paint heating contours on the model's upper fuselage and wings are presented in Figs. 4(c) and 7(c) for $\alpha = 25°$ and 40°, respectively. The corresponding oil-flow patterns were presented in Fig. 12. Heating on the upper fuselage at both angles of attack is characterized by two local maxima due to vortex reattachment on the leeward centerline, one near $x/L = 0.2$ and the other much farther aft. Reference 10 demonstrated a close relationship between axial variations in surface flow directions associated with the upper fuselage vortex reattachment, obtained from oil-flow measurements, and the distribution of heating along the leeward centerline. According to the results of that study, local heating increases as the local outward surface flow direction on the upper fuselage becomes larger. An examination of leeward fuselage surface flow directions in Figs. 12(a) and 12(b) show that the local heating maxima in Figs. 4(c) and 7(c) obey the same relationship. The heating peak near $x/L = 0.2$ at both 25° and 40° angle of attack corresponds to a region where there are relatively large angles between the oil-flow surface directions and the leeward centerline. A short distance aft of this region the surface flow directions become more nearly parallel to the leeward centerline, which should translate into a decrease in local heating. This is supported by the lack of melting in the phase change paint in Fig. 4(c) and 7(c) immediately aft of the initial heating peak. Surface flow directions for $\alpha = 25°$ in Fig. 12(a) then rise slowly and steadily until achieving a second local maximum divergence

from the leeward centerline close to x/L = 0.8. This corresponds to the location of the second upper fuselage heating peak in Fig. 4(c). At α = 40°, there is a similar correspondence between the second local maximum in flow angle in Fig. 12(b) and the second heating peak in Fig. 7(c) near x/L = 0.6. Wing heating contours in Fig. 4(c) show that flow reattachment resulting from shock-induced separation observed in oil flow near the wing's mid-section at α = 25° results in a relatively high heating rate over the affected area. There is also a suggestion that somewhat enhanced heating levels are caused by flow reattachment on the wing trailing edge near the fuselage and the tip fin. Very low heating rates exist over the inboard central portion of the wing upper surface. Heating rates at forward locations on the wing close to the fuselage at α = 40° in Fig. 7(c) are elevated apparently due to outflow from the side fuselage vortex. Undulations in isotherms 5 and 6 near the wing trailing edge may reflect the influence of flow reattachment noted at the same location in Fig. 13(b). Also, the notch in isotherm number 6 near the center of the wing planform seems to be related to the narrow slice of attached flow which thrusts in the aft direction between the complex separated region flow patterns near the mid-span in Fig. 12(b) and 13(b).

Figure 8 presents examples of heating contour data for $N_{Re,\infty}$ = 1.64 x 10^6 m^{-1} instead of 3.28 x 10^6 m^{-1}. This data is for α = 30 degrees and can be compared to Fig. 5. At a particular location on the windward side, h/h_o is only slightly less at the lower Reynolds number. Evidence of wing windward surface "streak" heating is more prevalent at the higher Reynolds number, however. The higher Reynolds number data in Fig. 5(c) show two areas of higher localized heating on the fuselage leeward centerline that are not seen in the lower Reynolds number data in Fig. 8(c).

Data presented in the previous figures provide detailed information about heating and surface flow over most of the model. Comparisons and trends in data can be better illustrated in graphical form, however. Figures 15 through 20 provide this information. Leeside heating along the fuselage centerline is represented in Fig. 15 as a function of angle of attack at $N_{Re,\infty}$ = 3.28 x 10^6 m^{-1}. The influence of α on heating level can be seen to vary depending on the axial location. Also, the location and magnitude of local "hot spots" as seen in the heating contour data (for example Fig. 6(c) are determined by the angle of attack. Regions of x/L without plotted data indicate that heating was insufficient to melt the phase-change paint. For the same test conditions, Fig. 16 depicts heating along the windward centerline. Although h/h_o is quite strongly a function of α, the values decrease sharply in the nose region and again in the wing region but are nearly constant over the cylindrical section. To put these data in perspective, consider the comparison of windward centerline heating on the present configuration (CBV) and the Space Shuttle Orbiter configuration shown in Fig. 17. The Orbiter data were obtained by the same technique, in the same wind tunnel, and at the same test conditions except for a difference of 2 degrees in angle of attack. The models were made of the same material and the lengths were approximately the same. The value of h_o based on a sphere diameter scaled to each full-size vehicle is presented in each case so that differences in model scale were accounted for. A theoretical prediction is also included for the Orbiter heating. The CBV and Shuttle Orbiter have nearly the same magnitude and distribution of nondimensionalized windward centerline heating. A similar comparison of lateral heating distribution at x/L = 0.4 is shown in Fig. 18. In this figure, the off-center heating values are compared to the respective centerline value for each configuration. The Orbiter heating rate data were taken directly from Ref. 11, and the CBV heat-transfer coefficient data were converted to q by use of Eq. 5 for direct comparison. The CBV configuration is cylindrical at this axial location and the heating decreases away from the centerline as expected. Because of the Orbiter wing glove, or strake, the relatively small corner radius results in an increase in heating between the centerline and outer edge of the vehicle.

Circumferential heating distributions around the CBV body at x/L = 0.2 and 0.6 are shown in Figs. 19 and 20, respectively for three angles of attack. At x/L = 0.2, corresponding to the ogive nose section, the windward heating increases with angle of attack and decreases with distance from the windward centerline. In the region of blending of the wing and body (x/L = 0.6) the CBV cross-section is somewhat Shuttle-like and the heating increases between the windward centerline and the wing-glove edge as shown in Fig. 20. Heating on the leading edge of the wing-glove, as on the leading edge of the wing, could not be determined by the phase-change paint technique since paint melt times were much too short to be useful. Based on Figs. 17 through 20, heating on the proposed full-scale CBV would not be dramatically different from that experienced by the present Shuttle Orbiter, so that existing thermal protection systems may be adequate for most of the structure. Of course, leading edge heating values were not obtained in this study but geometric similarity between CBV and Shuttle wings would suggest that the wing leading edge heating would not be vastly different between the two configurations. Heating along the leading edge of the wing tip fins was of interest but also could not be determined in these tests. Reference 12 reports a heat-transfer study that was carried out on a modified Shuttle Orbiter configuration with a wing tip fin. The tests were made in a shock tunnel and thin-film resistance thermometers were used to infer heating rate. At Mach 10 and α = 28°, tip-fin leading edge heating was found to be on the order of five times the maximum heating on the sides of the fin. However, leading edge heating decreased with increasing angle of attack. Wing shock impingement was found to be a major source of tip-fin leading edge heating. Because of geometric similarities, CBV tip-fin leading edge heating is probably subject to similar relationships.

Conclusions

A 0.0055-scale model of a single-stage-to-orbit transport vehicle with a circular body configuration was tested at Mach 10 to obtain heat transfer measurements and surface flow patterns. Based on the results of these tests, the following concluding remarks are made.

Maximum heating occurred on the nose and leading edges of the wing and tip fins, as expected, but values were not obtained for these areas because paint melt times were too short. When size was accounted for, the magnitude and distribution of heat-transfer coefficient along the windward centerline of the CBV were very similar to that obtained on the Space Shuttle Orbiter. Windward centerline heating decreased with decreasing angle of attack, but the distribution remained relatively constant. Forward of the wing, windward heating decreased rapidly off-centerline in the spanwise direction. Wing windward heating distributions were similar to the Shuttle Orbiter in the sense that chordwise streaks of higher heating were evident at lower angles of attack (25-deg) but were not evident at high angles of attack (40-deg). Oil-flow studies revealed a complicated leeside flowfield with flow separation, vortices, and reattachment that resulted in localized hot spots on the upper fuselage. Overall, however, heating was sufficiently similar to the Space Shuttle Orbiter under the same conditions to suggest that existing thermal protection systems may be adequate for use on the proposed CBV.

References

[1]Jones, Robert A. and Hunt, James L., "Use of Fusible Temperature Indicators for Obtaining Quantitative Aerodynamic Heat Transfer Data," NASA TR R-230, 1966.

[2]Creel, Theodore R., "A Device for Rapid Determination of Thermophysical Properties of Phase-Change Wind-Tunnel Models," NASA TM X-3421, 1976.

[3]Hunt, James L., Pitts, Joan I., and Richie, Christine B., "Application of Phase-Change Technique to Thin Sections with Heating on Both Surfaces," NASA TN D-7193, 1973.

[4]Wells, William L., "Heating Measurements on Space Shuttle Orbiter Models with Differentially Deflected Elevons," NASA TM 84646, 1983.

[5]Shaefer, W. T., Jr., "Characteristics of Major Active Wind tunnels at the Langley Research Center," NASA TM X-1130, 1965.

[6]Edney, Barry, "Anomalous Heat Transfer and Pressure Distributions on Blunt Bodies at Hypersonic Speeds in the Presence of an Impinging Shock," FFA Report 115. Aeronautical Research Institute of Sweden, 1968.

[7]Seegmiller, H. Lee, "Surface-Flow Visualization Investigation of a High Cross Range Shuttle Configuration at a Mach Number of 7.4 and Several Reynolds Numbers," NASA TM X-62036, 1970.

[8]Black, L. H. and Cuffel, R. J., "Changes in Heat Transfer from Turbulent Boundary Layers Interacting with Shock Waves and Expansion Waves," AIAA Journal, Vol. 8, No. 10, pp. 1871-1873, October 1970.

[9]Helms, Vernon T. III, "Oil Flow Study of Space Shuttle Orbiter Tip-Fin Controller," NASA TM 86276, 1984.

[10]Helms, Vernon T. III, "An Empirical Method for Computing Leeside Centerline Heating on the Space Shuttle Orbiter," Journal of Spacecraft and Rockets, Vol. 20, No. 3, May-June 1983.

[11]Hamilton, Harris H. II, "Approximate Method of Predicting Heating on the Windward Side of Space Shuttle Orbiter and Comparisons with Flight Data," AIAA Paper 82-0823, June 1982.

[12]Wittliff, Charles E., "A Study of Aerodynamic Heating Distributions on a Tip-Fin Controller Installed on a Space Shuttle Orbiter Model," NASA CR 166025, 1982.

Table 1. Scope of tests in Langley 31-Inch Mach-10 Tunnel.

M_∞	P_t	T_t	$N_{Re,\infty}$	α	* h_o	Tests	
-	(kPa)	(K)	(m^{-1})	(Degrees)	W/cm^2K	Heat Transfer	Oil Flow
10.02	4964.2	1000	3.28×10^6	20,25,30,35,40	0.110	X	X
9.86	2413.2	1000	1.62×10^6	30	0.080	X	

*Scaled to the CBV

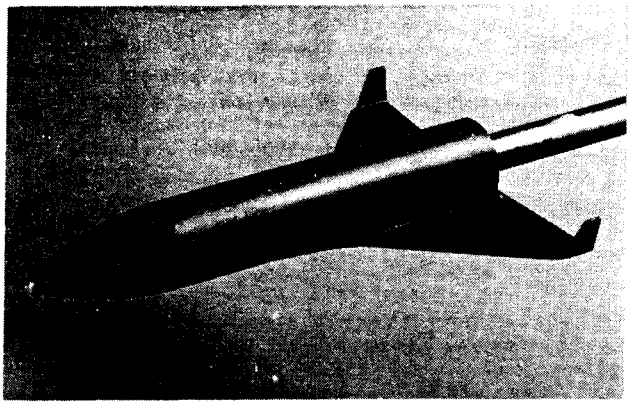

(a) Photograph of stycast model.

Fig. 1 Wind tunnel model of proposed single-stage-to-orbit, circular body vehicle.

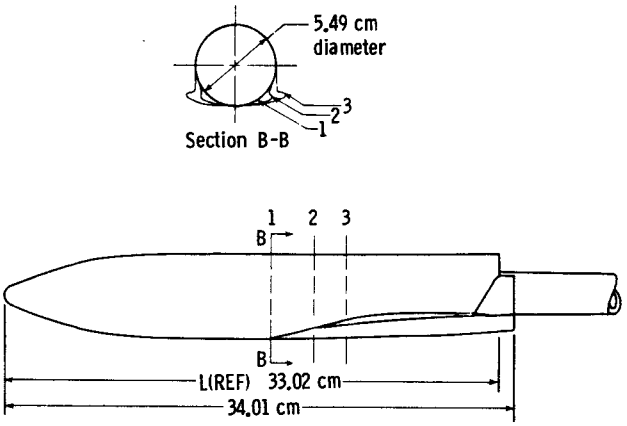

(c) Side view drawing.

Fig. 1 Continued.

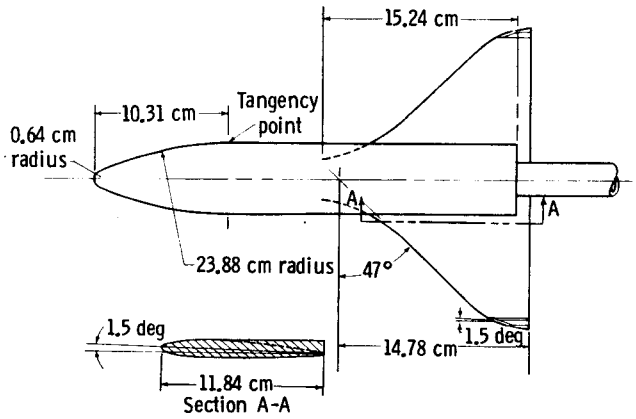

(b) Top view drawing.

Fig. 1 Continued.

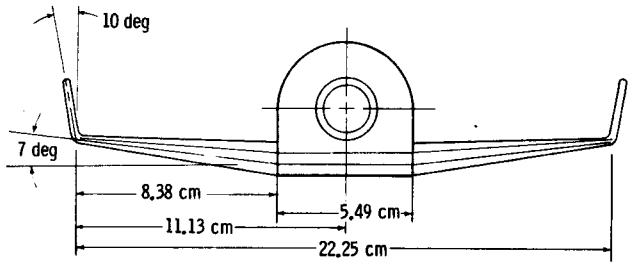

(d) Rear view drawing.

Fig. 1 Concluded.

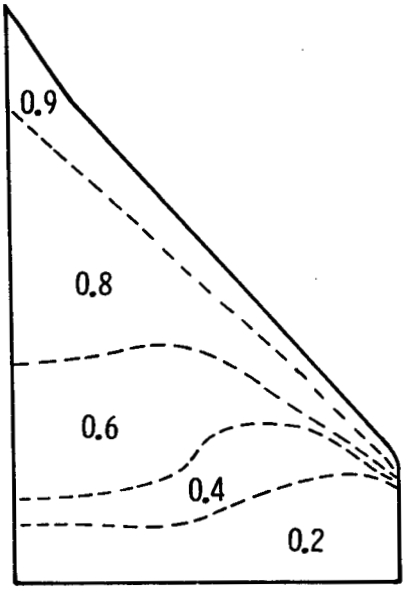

Fig. 2 Wing upper surface multiplying factors, f for h/h_o.

Isotherm	Body h/h_o	Fin h/h_o
1	.0391	.0334
2	.0276	.0218
3	.0226	.0160
4	.0175	
5	.0148	
6	.0124	
7	.0104	

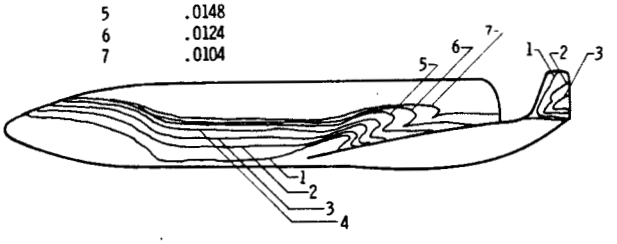

(b) Side view.

Fig. 3 Continued.

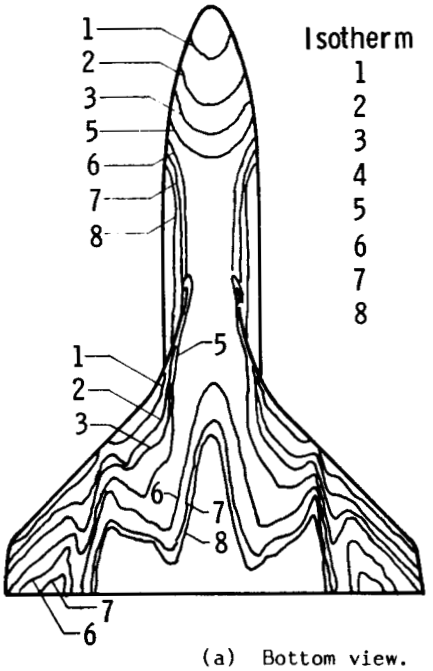

Isotherm	h/h_o
1	.0999
2	.0706
3	.0577
4	.0500
5	.0447
6	.0378
7	.0316
8	.0277

(a) Bottom view.

Fig. 3 Heat-transfer coefficient contour map of model at M = 10, $N_{Re,\infty}$ = 3.28 x 10^5 m^{-1}, and α = 20 deg.

Isotherm	h/h_o	$(h/h_o)/f$
1	.027	.0300
2	.012	.0212
3	<.008	.0150
4	<.006	.0122
5	.005	.0100
6	<.003	.0090
7	<.002	.0083
8	—	.0077

f = 1 on fuselage

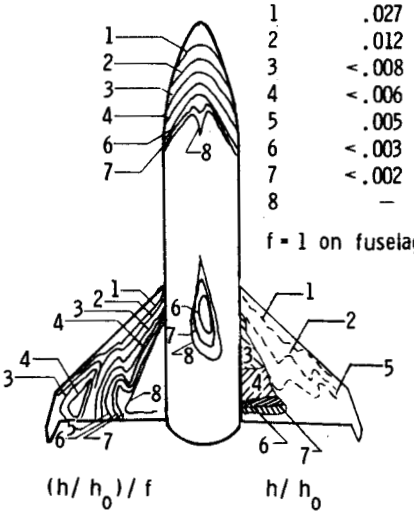

(c) Top view.

Fig. 3 Concluded.

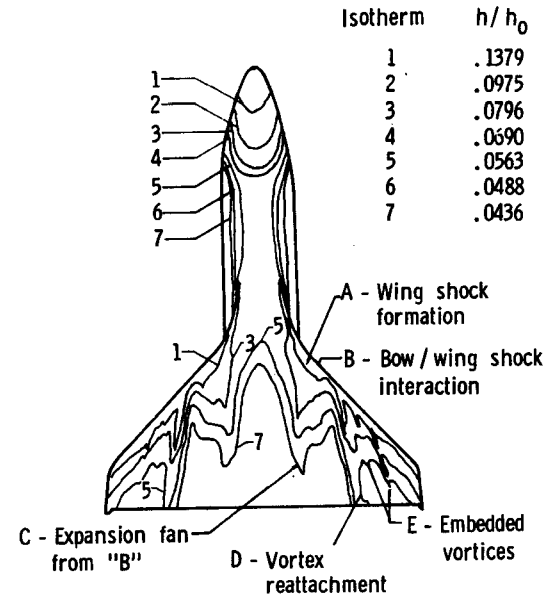

(a) Bottom view.

Fig. 4 Heat-transfer coefficient contour map of model at M = 10, $N_{Re,\infty}$ = 3.28 x 10^6 m^{-1}, and α = 25 deg.

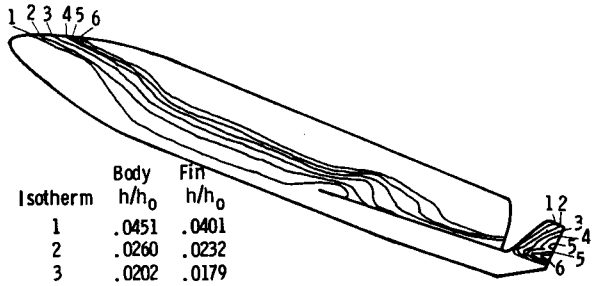

Isotherm	Body h/h_0	Fin h/h_0
1	.0451	.0401
2	.0260	.0232
3	.0202	.0179
4	.0170	.0152
5	.0143	.0127
6	.0125	.0111

(b) Side view.

Fig. 4 Continued.

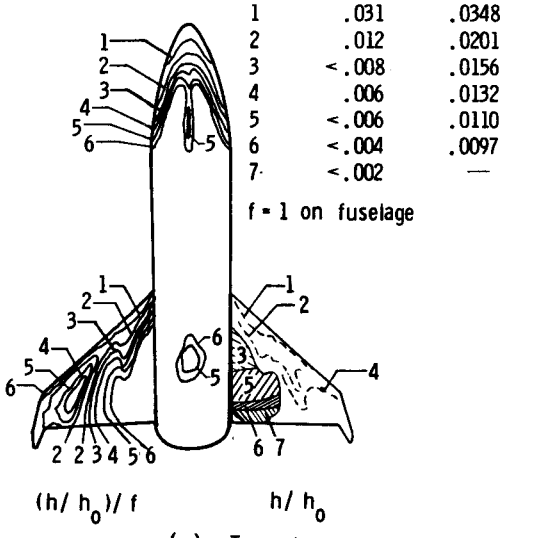

(c) Top view.

Fig. 4 Concluded.

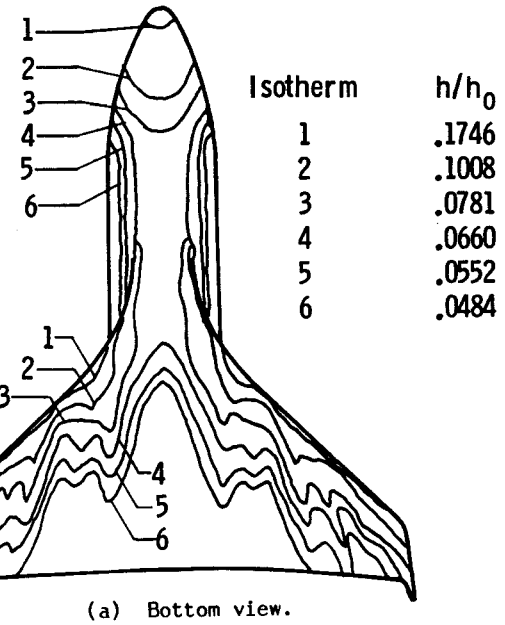

(a) Bottom view.

Fig. 5 Heat-transfer coefficient contour map of model at M = 10, $N_{Re,\infty}$ = 3.28 x 10^6 m^{-1}, and α = 30 deg.

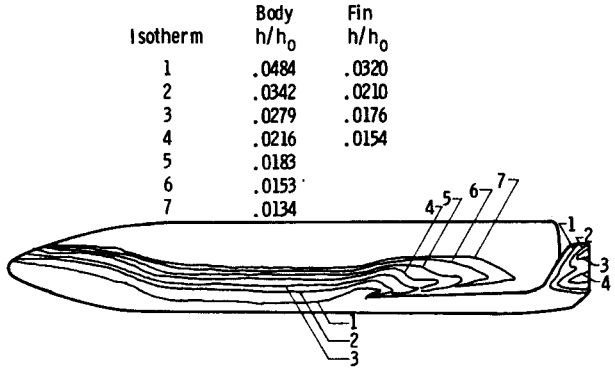

Isotherm	Body h/h_0	Fin h/h_0
1	.0484	.0320
2	.0342	.0210
3	.0279	.0176
4	.0216	.0154
5	.0183	
6	.0153	
7	.0134	

(b) Side view.

Fig. 5 Continued.

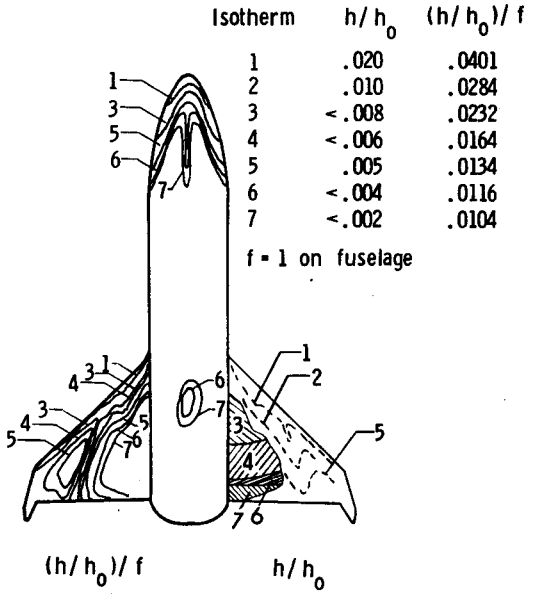

(c) Top view.

Fig. 5 Concluded.

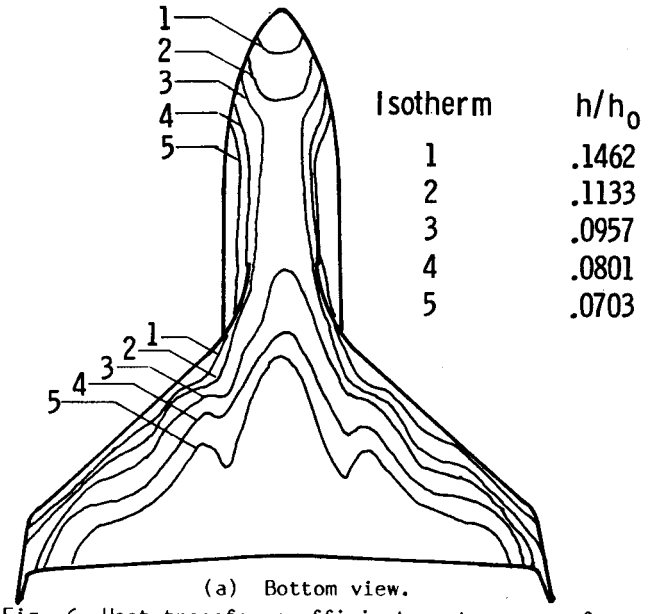

(a) Bottom view.

Fig. 6 Heat-transfer coefficient contour map of model at M = 10, $N_{Re,\infty}$ = 3.28 x 10^6 m^{-1}, and α = 35 deg.

Isotherm	Body h/h_0	Fin h/h_0
1	.0376	.0392
2	.0266	.0248
3	.0217	.0210
4	.0168	.0154
5	.0142	
6	.0119	
7	.0104	

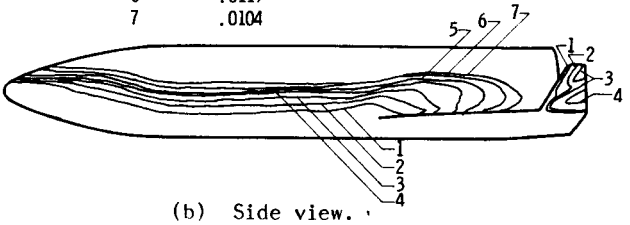

(b) Side view.

Fig. 6 Continued.

Isotherm	h/h_0	$(h/h_0)/f$
1	.017	.0332
2	.010	.0192
3	<.007	.0148
4	<.005	.0125
5	.005	.0105
6	<.004	.0092
7	<.002	—

f = 1 on fuselage

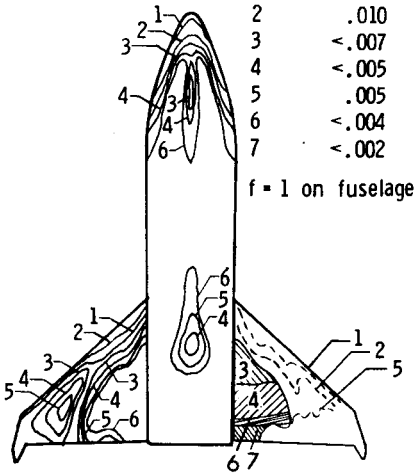

$(h/h_0)/f$ h/h_0

(c) Top view.

Fig. 6 Concluded.

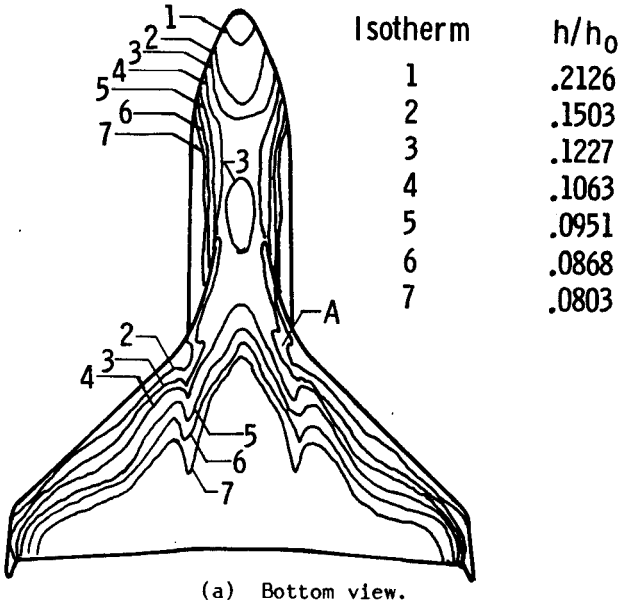

(a) Bottom view.

Fig. 7 Heat-transfer coefficient contour map of model at M = 10, $N_{Re,\infty}$ = 3.28 x 10^6 m^{-1}, and α = 40 deg.

Isotherm	Body h/h_0	Fin h/h_0
1	.0319	.0540
2	.0226	.0312
3	.0194	.0242
4	.0143	.0150
5	.0121	

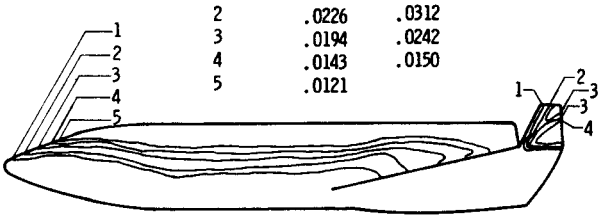

(b) Side view.

Fig. 7 Continued.

Isotherm	h/h_0	$(h/h_0)/f$
1	.018	.0348
2	.010	.0201
3	<.008	.0156
4	<.006	.0132
5	<.004	.0110
6	.003	.0097
7	.002	—

f = 1 on fuselage

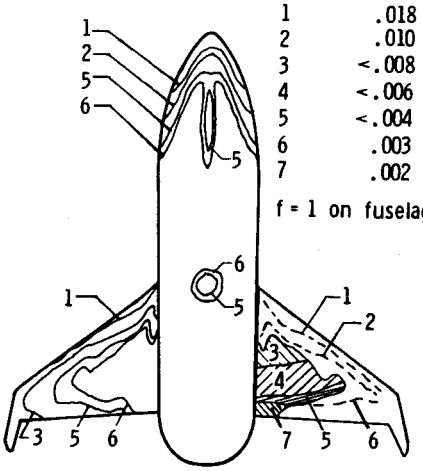

$(h/h_0)/f$ h/h_0

(c) Top view.

Fig. 7 Concluded.

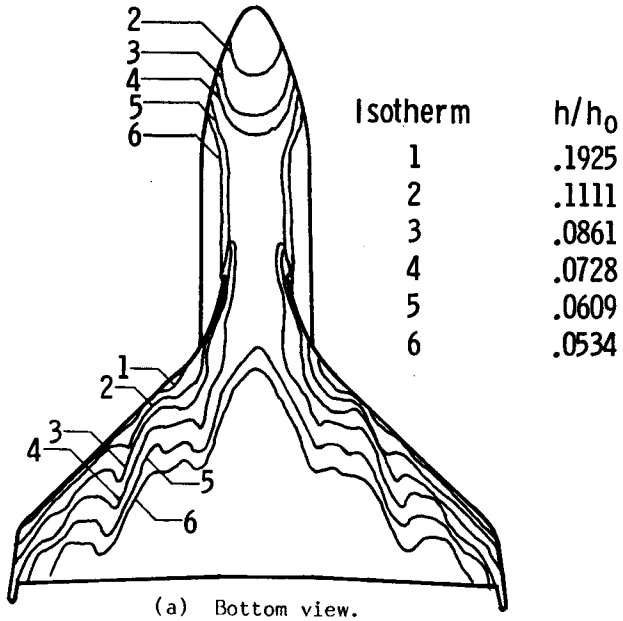

(a) Bottom view.

Fig. 8 Heat-transfer coefficient contour map of model at M = 10, $N_{Re,\infty}$ = 1.64 x 10^6 m^{-1}, and α = 30 deg.

Isotherm	Body h/h_0	Fin h/h_0
1	.0590	.0356
2	.0341	.0234
3	.0264	.0171
4	.0223	
5	.0187	
6	.0164	

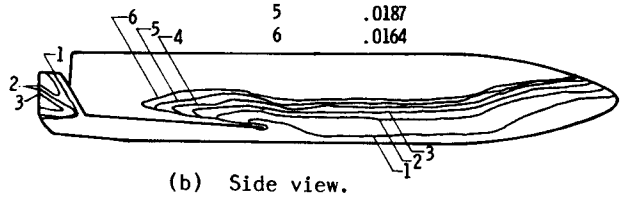

(b) Side view.

Fig. 8 Continued.

Isotherm	h/h_0	$(h/h_0)/f$
1	.046	.0515
2	.015	.0297
3	<.011	.0230
4	<.009	.0195
5	.009	.0163
6	<.006	.0143
7	<.003	

f = 1 on fuselage

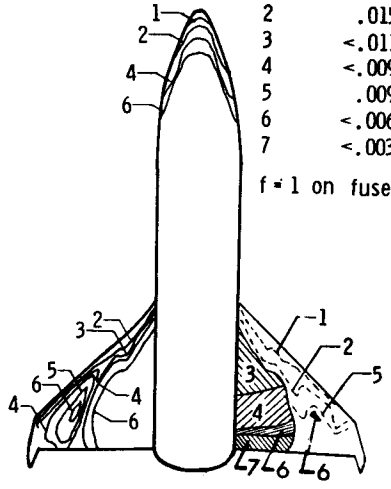

(c) Top view.

Fig. 8 Concluded.

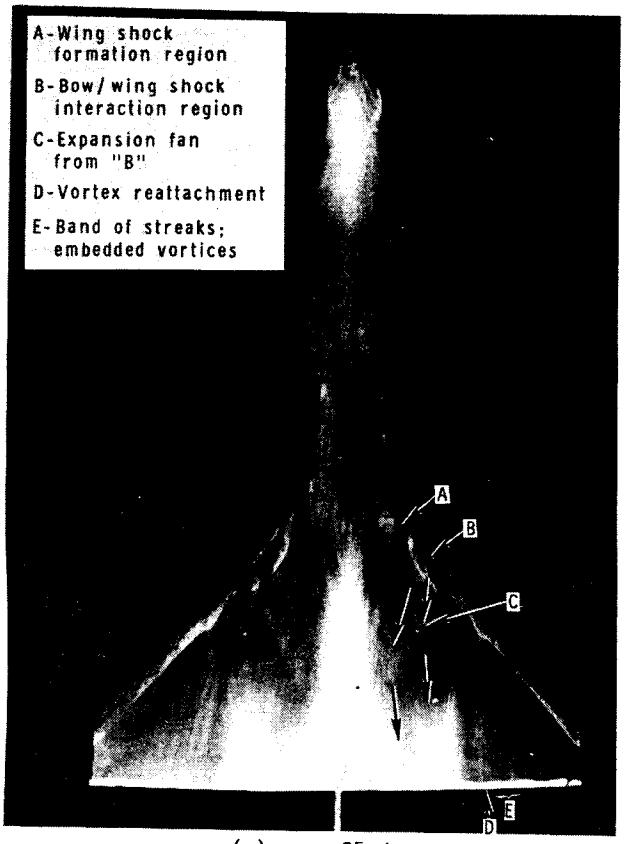

(a) α = 25 deg.

Fig. 9 Windwward oil-flow on CBV model at M = 10, $N_{Re,\infty}$ = 3.28 x 10^6 m^{-1}.

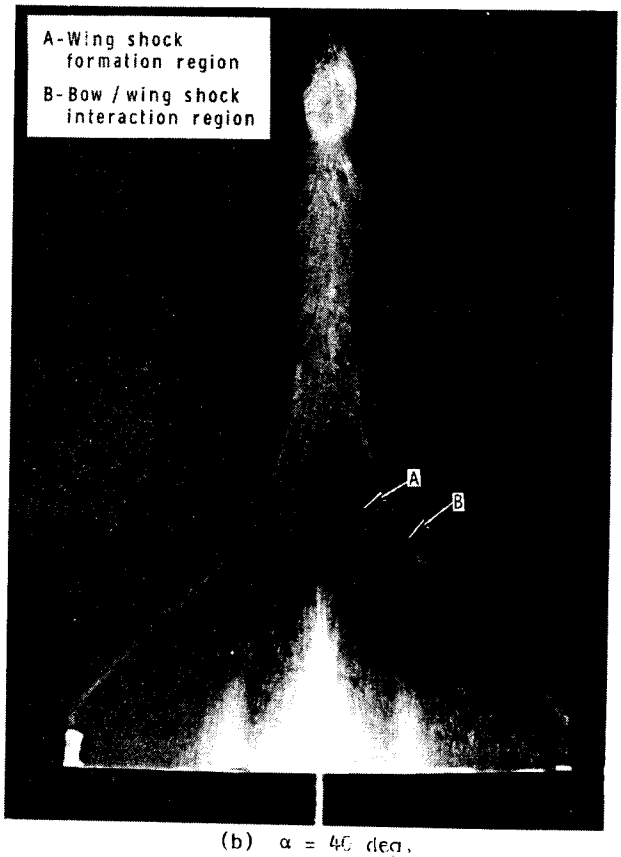

(b) α = 40 deg.

Fig. 9 Concluded.

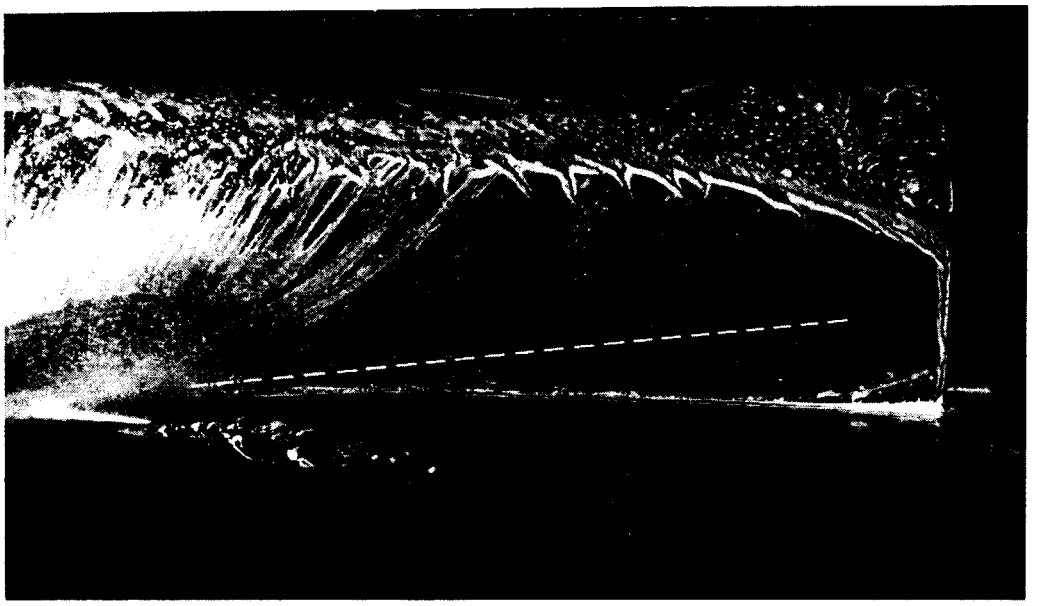

(a) α = 25 deg.

Fig. 10 Oil flow on side fuselage, above wing at M = 10, $N_{Re,\infty} = 3.28 \times 10^6$ m^{-1}.

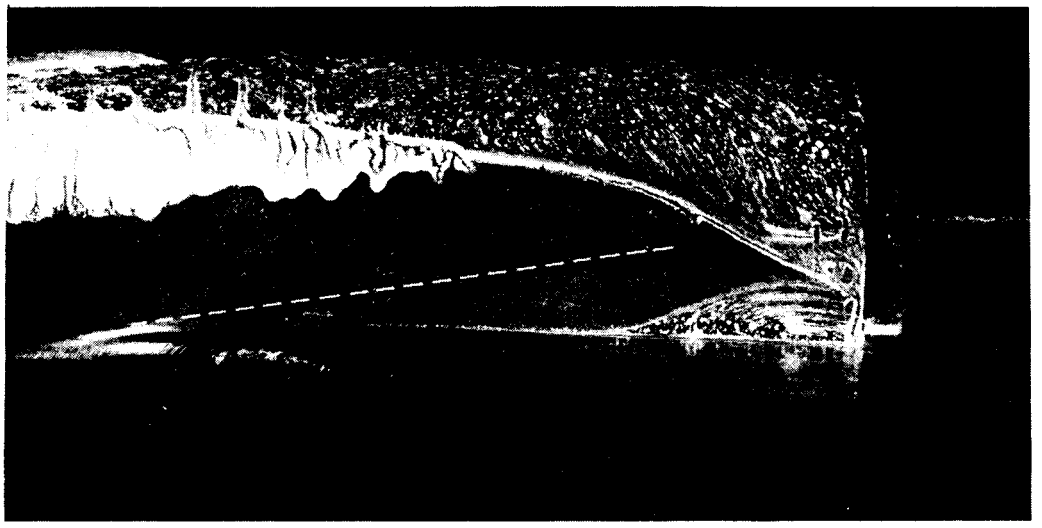

(b) α = 40 deg.

Fig. 10 Continued.

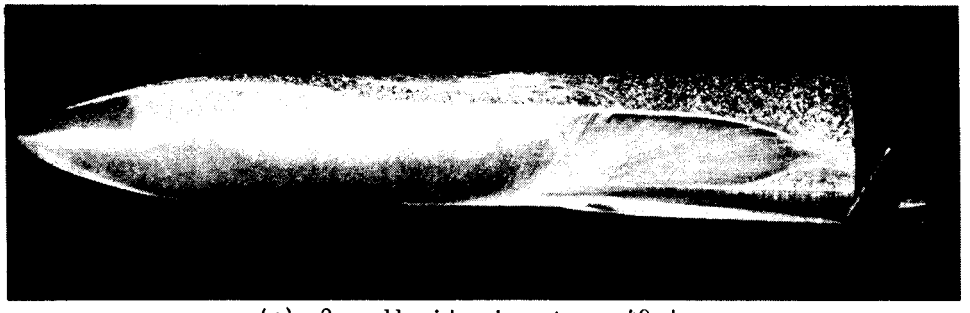

(c) Overall side view at α = 40 deg.

Fig. 10 Concluded.

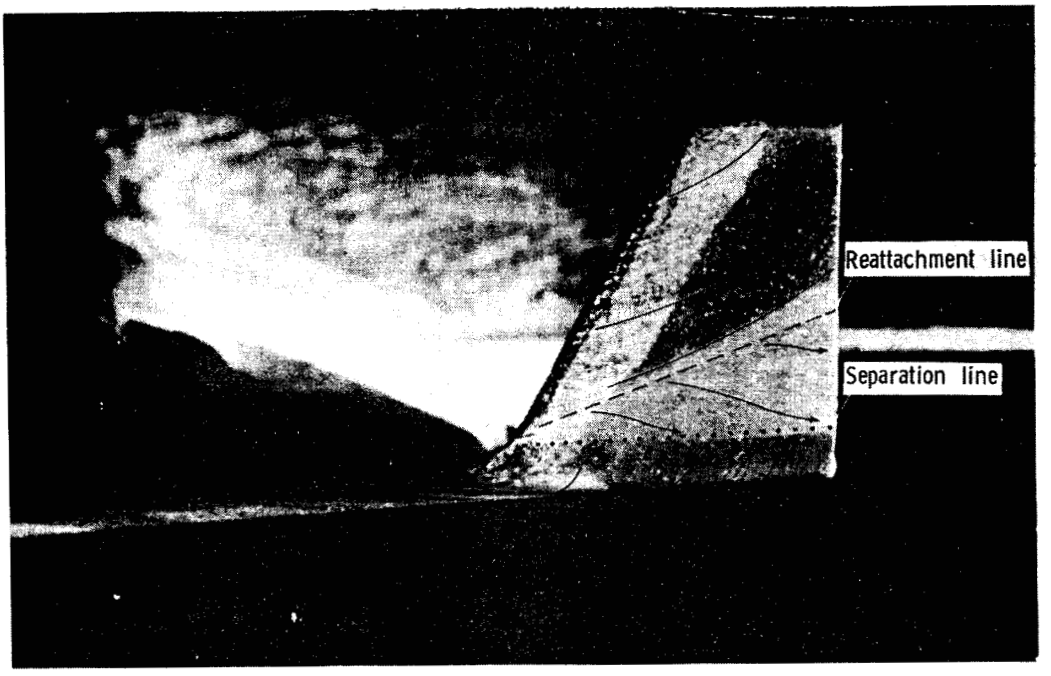

(a) α = 25 deg.

Fig. 11 Oil flow on wing tip-fin at M = 10 and $N_{Re,\infty} = 3.28 \times 10^6$ m^{-1}.

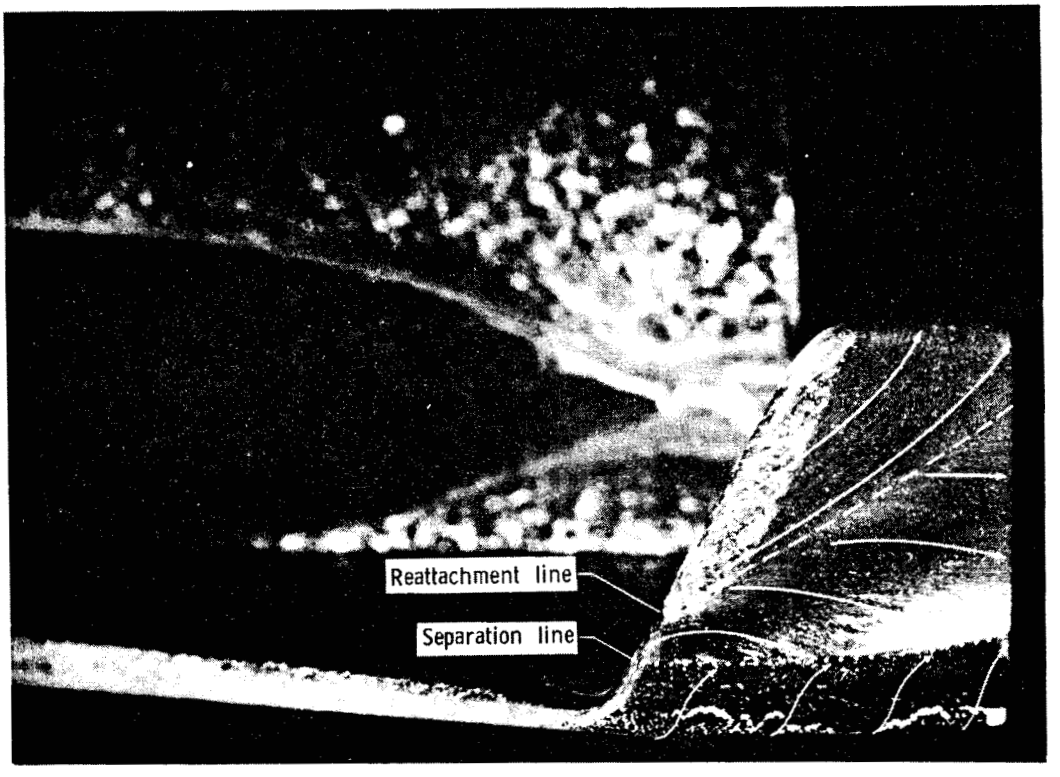

(b) α = 40 deg.

Fig. 11 Concluded.

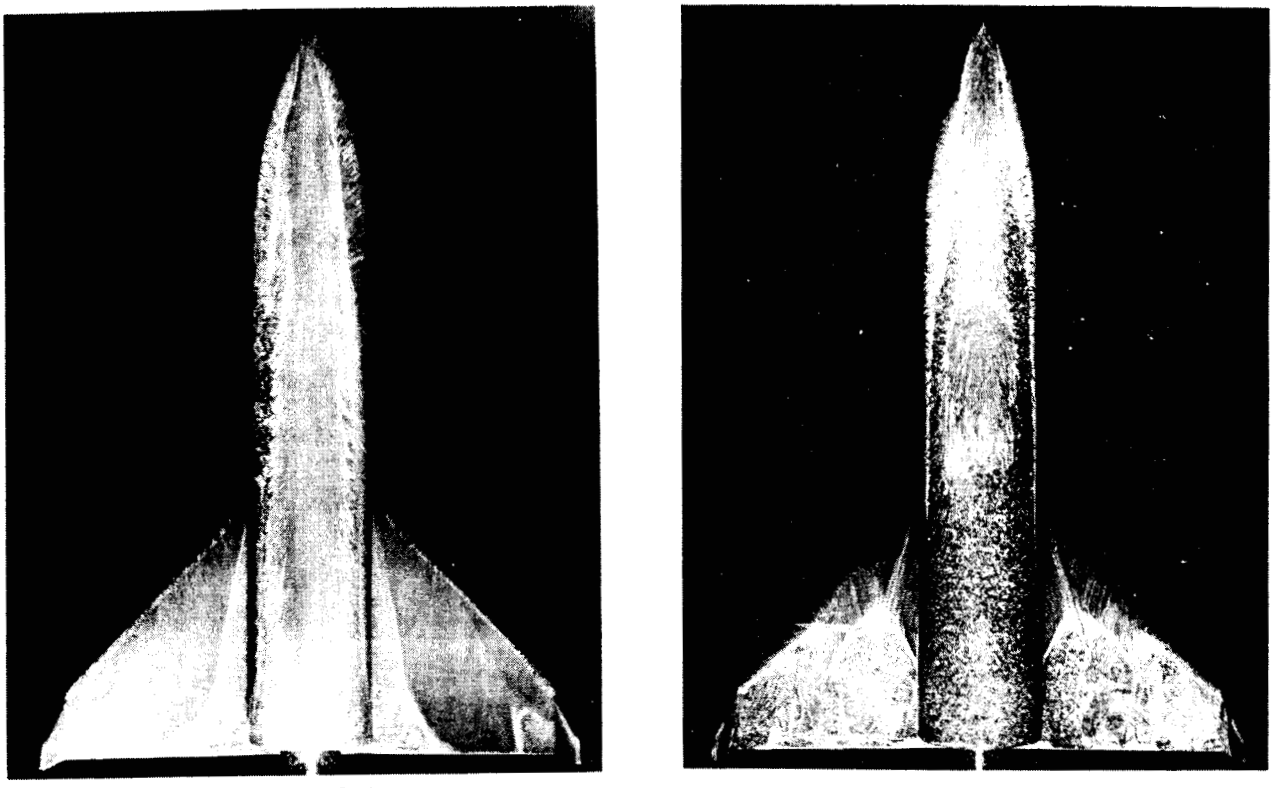

(a) α = 25 deg. (b) α = 40 deg.

Fig. 12 Oil flow on CBV model leeside at M = 10 and $N_{Re,\infty} = 3.28 \times 10^6$ m^{-1}.

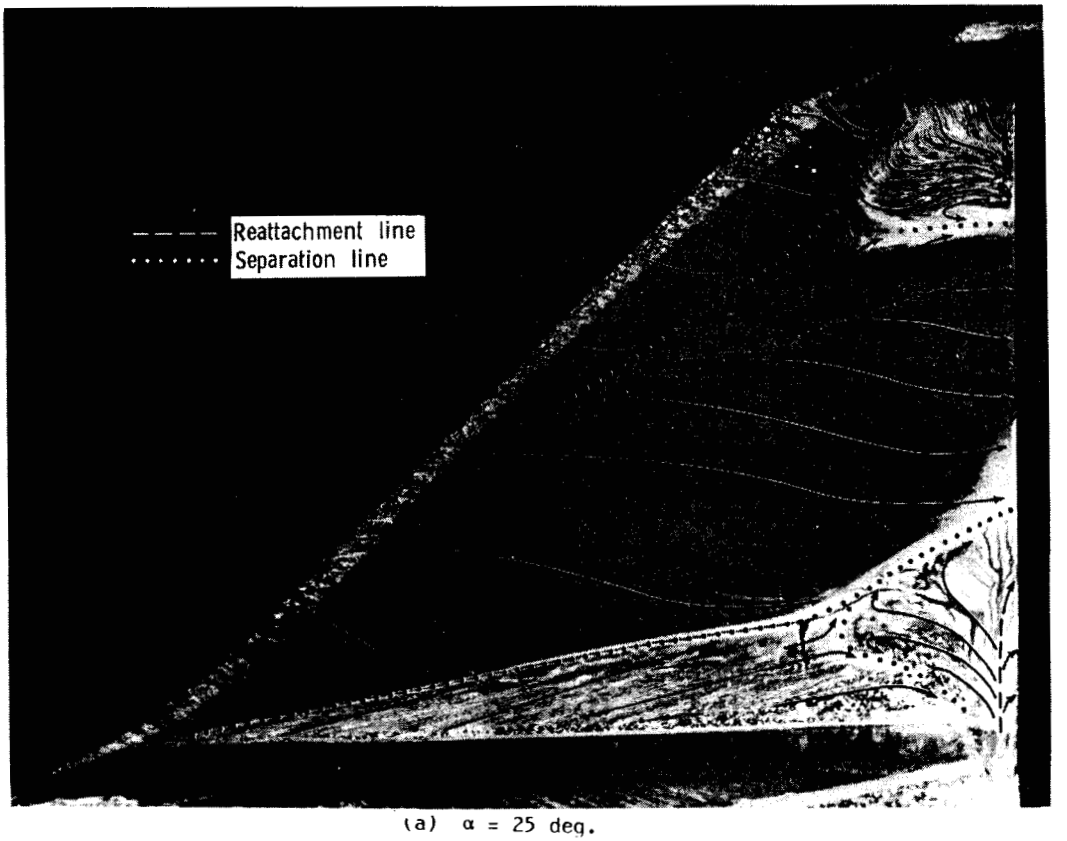

(a) α = 25 deg.

Fig. 13 Wing leeside oil flow at M = 10 and $N_{Re,\infty} = 3.28 \times 10^6$ m^{-1}.

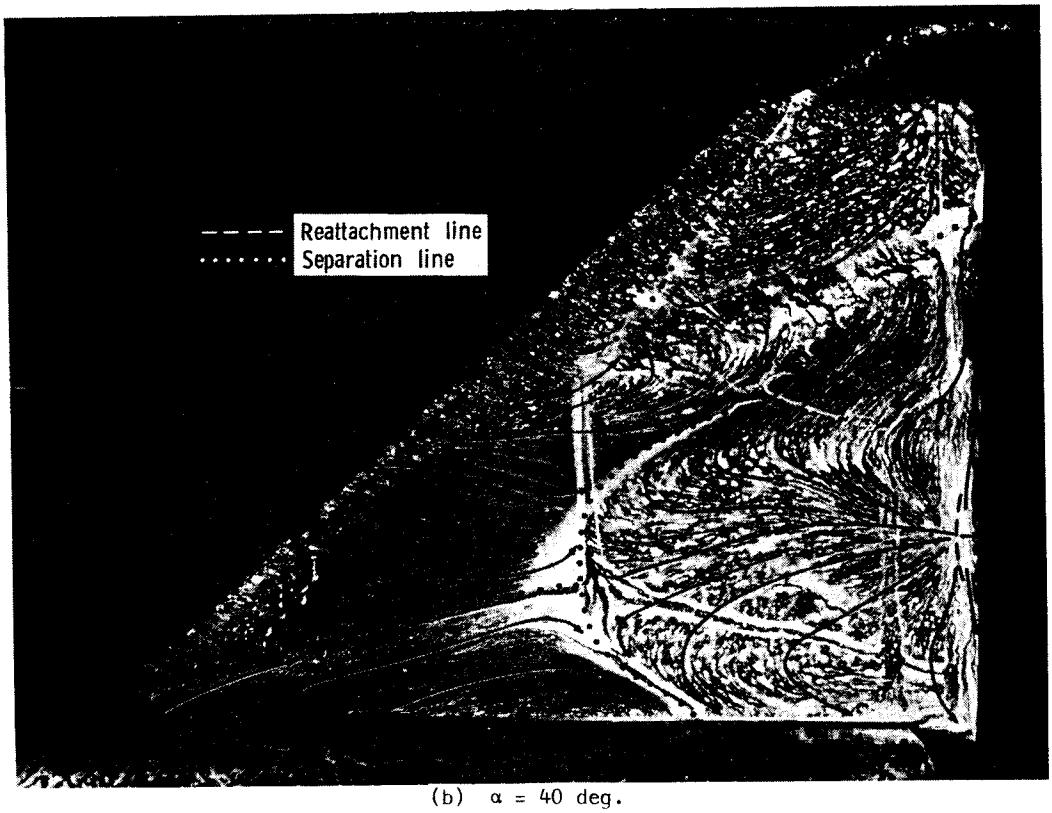

(b) α = 40 deg.

Fig. 13 Concluded.

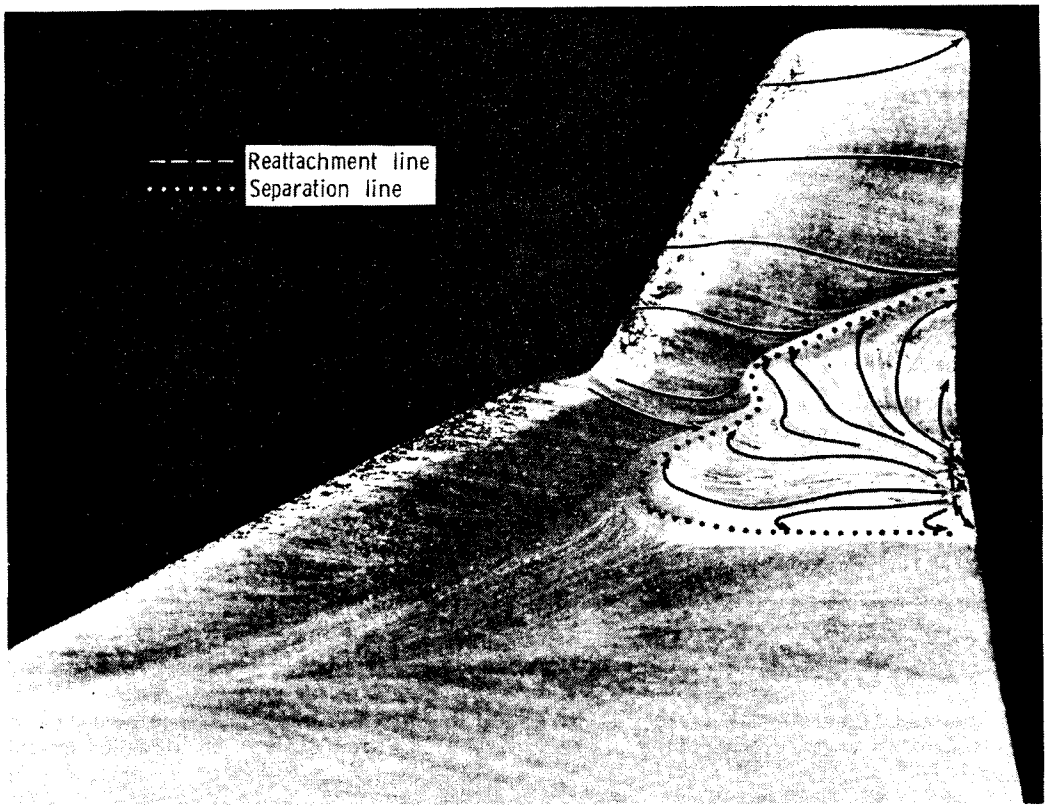

(a) α = 25 deg.

Fig 14 Oil flow near wing and tip-fin juncture at M = 10, $N_{Re,\infty}$ = 3.28 x 10^6 m^{-1}.

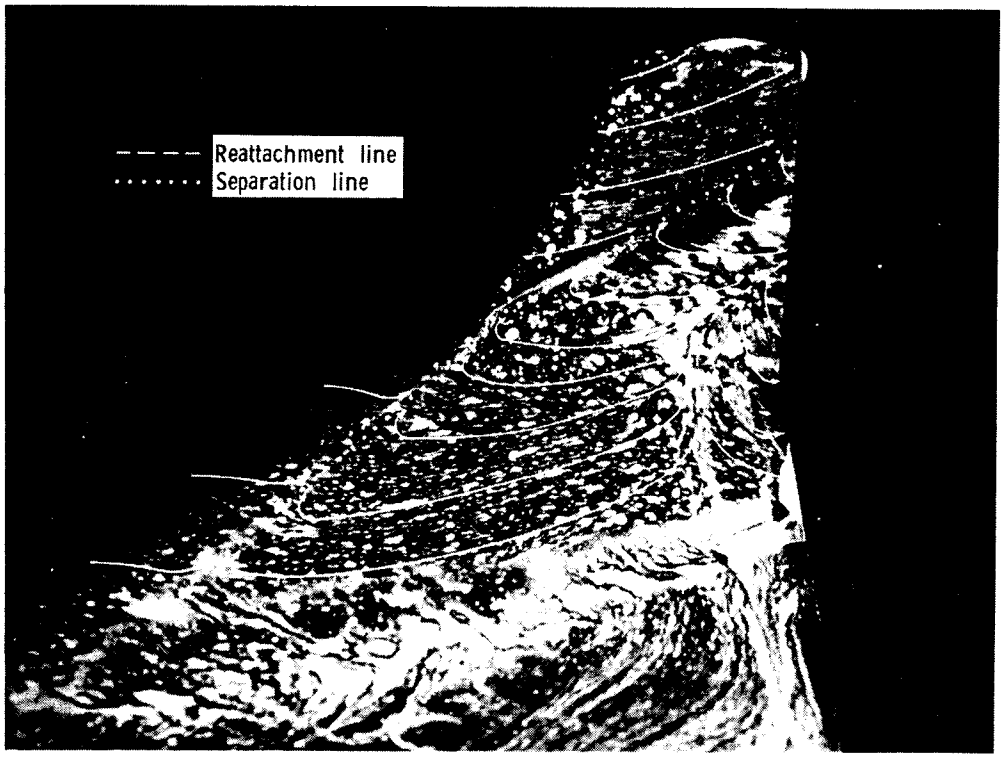

(b) α = 40 deg.

Fig. 14 Concluded.

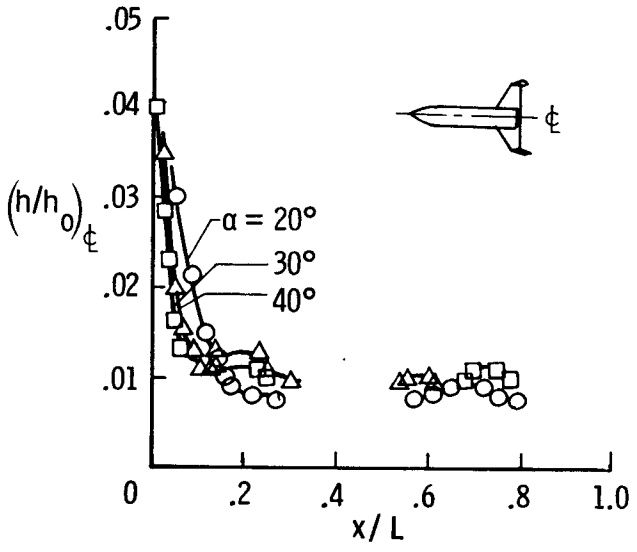

Fig. 15 Nondimensionalized heat-transfer coefficient on leeward centerline at $N_{Re,\infty}$ = 3.28 x 10^6 m^{-1}, M = 10.

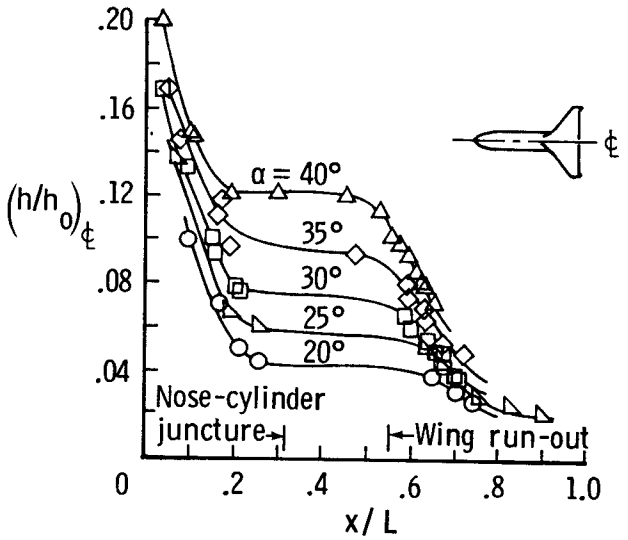

Fig. 16 Nondimensionalized heat-transfer coefficient on windward centerline at $N_{Re,\infty}$ = 3.28 x 10^6 m^{-1}, M = 10.

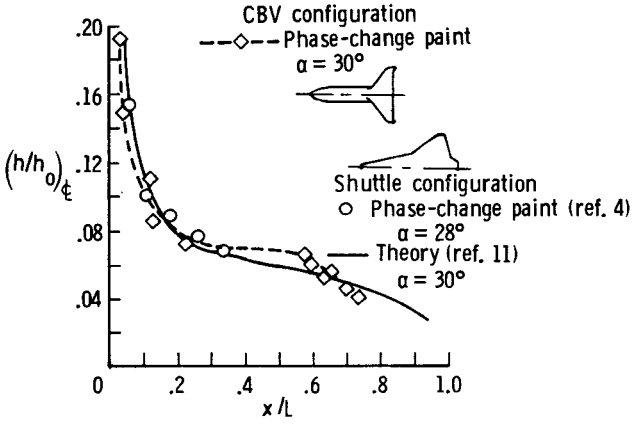

Fig. 17 Comparison of Space Shuttle Orbiter and CBV configurations windward centerline heat-transfer coefficient distributions at M = 10 and $N_{Re,\infty} = 1.64 \times 10^6$ m^{-1}.

(Shuttle $h_o = 0.059 \frac{W}{cm^2 K}$; CBV $h_o = 0.081 \frac{W}{cm^2 K}$)

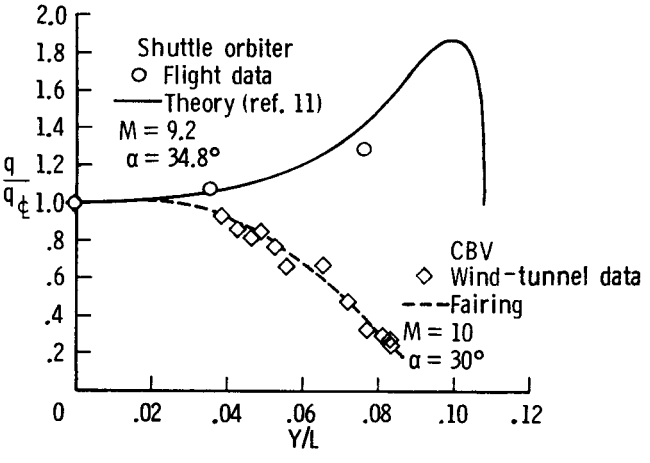

Fig. 18 Comparison of nondimensionalized windward heating distribution on Shuttle and CBV configurations at x/L = 0.4.

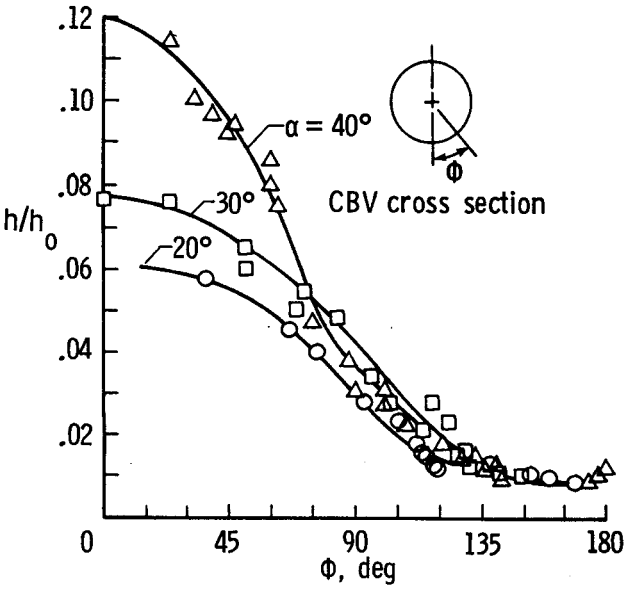

Fig. 19 Nondimensionalized heat-transfer coefficient circumferential distribution on CBV ogive section at x/L = 0.2, M = 10; $N_{Re,\infty} = 3.28 \times 10^6$ m^{-1}.

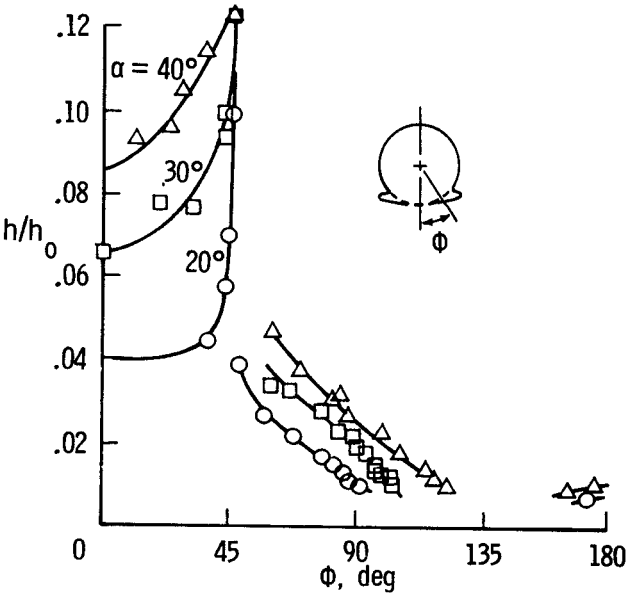

Fig. 20 Nondimensionalized heat-transfer coefficient circumferential distribution on CBV at $x/L_1 = 0.6$, M = 10, $N_{Re,\infty} = 3.28 \times 10^6$ m^{-1}.